

## Article

# Controllable and Scalable Fabrication of Superhydrophobic Hierarchical Structures for Water Energy Harvesting

Meiling Guo <sup>1</sup>, Cheng Wang <sup>1</sup>, Zhenchao Yang <sup>1,\*</sup>, Zhentao Xu <sup>1</sup>, Mingshun Yang <sup>1</sup>, Pengkang Zhao <sup>1</sup>, Yan Zhou <sup>2</sup>, Pengyang Li <sup>1</sup>, Quandai Wang <sup>1</sup> and Yan Li <sup>1</sup>

<sup>1</sup> School of Mechanical and Precision Instrument Engineering, Xi'an University of Technology, Xi'an 710048, China; guomeiling@xaut.edu.cn (M.G.); wangchengedz@163.com (C.W.); 18339695177@yeah.net (Z.X.); yangmingshun@xaut.edu.cn (M.Y.); zhaopengkang@xaut.edu.cn (P.Z.); lipengyang@xaut.edu.cn (P.L.); quandaiw@163.com (Q.W.); jyxy-ly@xaut.edu.cn (Y.L.)

<sup>2</sup> School of Mechanical and Electrical Engineering, Guangzhou University, Guangzhou 510006, China; yanzhou@gzhu.edu.cn

\* Correspondence: zcyang@xaut.edu.cn; Tel.: +86-13772172074

**Abstract:** We report a controllable and scalable fabrication approach for the superhydrophobic hierarchical structures and demonstrate the excellent ability to harvest water energy when applied to water-solid contact triboelectric nanogenerator (TENG). A strategy combined with multiple photolithography and micromolding process was developed to accurately regulate the diameters and the center distances of the two-level micropillars. A variety of hierarchical structures were successfully fabricated and presented the advantages of structure control, large scale, high accuracy, and high consistency. The hydrophobic property characterizations were conducted, and the results indicated that the hierarchical structures showed a larger contact angle than the single-level structures and achieved superhydrophobicity. Then the hierarchical structures were applied to water-TENGs with flowing water continuously dripping on, and the effect of the structure parameter on the triboelectric output was analyzed. The hierarchical structures exhibited a superior ability to harvest water energy than the flat film and the single-level structures due to the enhanced friction area and superhydrophobic property. At a flowing velocity of 8 mL/s, the hierarchical structure generated the output voltage of approximately 34 V and the short-circuit current of around 5  $\mu$ A. The water-TENG device exhibited a power density peak of 7.56  $\mu$ W/cm<sup>2</sup> with a resistive load of 16.6 M $\Omega$  at a flowing velocity of 10 mL/s. These findings shed light on the potential applications of the hierarchical structures-based water-TENGs to water energy harvesting and self-powered sensor devices.



**Citation:** Guo, M.; Wang, C.; Yang, Z.; Xu, Z.; Yang, M.; Zhao, P.; Zhou, Y.; Li, P.; Wang, Q.; Li, Y. Controllable and Scalable Fabrication of Superhydrophobic Hierarchical Structures for Water Energy Harvesting. *Electronics* **2022**, *11*, 1651. <https://doi.org/10.3390/electronics11101651>

Academic Editor: Dongseok Suh

Received: 30 March 2022

Accepted: 18 May 2022

Published: 22 May 2022

**Publisher's Note:** MDPI stays neutral with regard to jurisdictional claims in published maps and institutional affiliations.



**Copyright:** © 2022 by the authors. Licensee MDPI, Basel, Switzerland. This article is an open access article distributed under the terms and conditions of the Creative Commons Attribution (CC BY) license (<https://creativecommons.org/licenses/by/4.0/>).

## 1. Introduction

The massive development of electronic devices increases the demand for power sources. The energy supply for the wide-distributed, miniaturized, portable, and wearable electronic devices attracts considerable attention [1–3]. The traditional battery energy supply strategy suffers from its huge volume, short service time, natural resource consumption, and environmental pollution, making the development of green renewable energy sources extremely urgent [4,5]. Piezoelectric technology and triboelectric technology have been proposed to convert mechanical energy to electrical energy from environmental and biomechanical movements to power portable wearable electronic devices and mobile [6–9]. The triboelectric nanogenerator (TENG), using the coupling effects of contact triboelectrification and electrostatic induction, has drawn widespread attention due to its cost-effectiveness, simple fabrication, and high efficiency [10–12]. It can convert diverse types of mechanical energy into electricity, including human motion [13,14], vibration [15], wind [16], and flowing water [17,18]. Most recently, by virtue of inexhaustibility, wide distribution, and

green renewable energy, the water-solid contact TENG which can harvest water energy, has become a research hotspot.

In principle, constructing superhydrophobic micro/nanostructures is crucial for improving the triboelectric output of water-solid contact TENG [19–25]. On the one hand, the fabrication of micro/nanostructures would enlarge the friction area and then enhance the triboelectric charge density [19–21]. On the other hand, the superhydrophobic surface facilitates the complete and rapid removal of water drops, resulting in a more and faster charge transfer [22–25]. Various methods for fabricating superhydrophobic hierarchical structures have been developed [26–33]. Our previous work proposed a scalable electrospinning technology to create the hierarchical micro-nanostructures featured with superhydrophobicity, good transparency, and full stretchability for applications in harvesting mechanical energy and water energy [28]. Ahn et al. produced a wrinkled micro-nano hierarchical structure using a fabrication method combining nanotransfer, molding, and the buckling effect. This rough surface exhibited an excellent contact angle of 152.5° and enhanced triboelectric effects [29]. Employing the patterned Si wafers or natural structures as templates to fabricate micro/nano 3D patterns was also found to be a very efficient method to enlarge the effective contact area of triboelectric surfaces and improve output performance [30,31]. In addition to physics methods, chemical reactions and chemical etching were also employed to fabricate hierarchical structures. The significance of the hierarchical structure on durable and stable output generation of superhydrophobic TENG was suggested [32]. However, the structure of these hierarchical surfaces cannot be regulated precisely and conveniently, such as the sizes of pillars, pores, and wires. The influence of the hierarchical structure parameter on the triboelectric output of TENG is still unrevealed.

Herein, we proposed a photolithography and micromolding method to realize the well-controlled and scalable manufacturing of the superhydrophobic hierarchical structures. The sizes of the hierarchical micropillars could be regulated accurately and conveniently by changing the masks. The hydrophobic property characterizations showed that the hierarchical structures possessed a larger contact angle compared with the single-level micropillar arrays and achieved superhydrophobicity. For studying the application of the hierarchical structures to water-TENGs, a testing setup of water dripping onto the hierarchical structures was constructed. The triboelectric outputs of the flat film, the single-level structures, and the hierarchical structures at the constant flowing velocity were compared. The results indicated that the hierarchical surfaces exhibited a superior ability to harvest water energy, attributed to the enhanced friction area and superhydrophobic property. In addition, the effect of the primary micropillar center distance on the output performance of water-TENGs was explored and found to be consistent with the change of the hydrophobic property, demonstrating the significant contribution of superhydrophobicity to water energy harvesting.

## 2. Experimental Section

### 2.1. Fabrication of Hierarchical Structures

Figure 1 shows the fabrication process of the polydimethylsiloxane (PDMS) hierarchical structures using photolithography and the micromolding process. First, the PDMS secondary structures with micropillar arrays were fabricated using the conventional exposure, development, and molding process, as shown in Figure S1. The thicknesses of the fabricated PDMS secondary structures were 7  $\mu\text{m}$ . Second, the secondary structure templates with microhole arrays were fabricated by negatively duplicating the PDMS secondary structures using UV imprinting lithography, as shown in Figure 1a–c. A NOA71 UV-cured polymer with fast curing and long-term stability over a wide temperature range was chosen as the imprinted material. It was spin-coated on the glass slide with a speed of 1000 rpm for 60 s, and the PDMS secondary structure template was pressed onto this slide (Figure 1a). Following this, the whole wafer was cured under UV light with a wavelength of 350 nm for 10 min (Figure 1b). After demolding, the corresponding UV-cured polymer microholes were obtained as the secondary structure template (Figure 1c). Third, taking the

UV-cured polymer microhole template as the substrate, the PDMS hierarchical structures were fabricated by the second exposure, development, and molding process, as shown in Figure 1d–h. A SU8-2050 negative photoresist was spun on the substrate containing the UV-cured polymer microhole array at 1600 rpm for 35 s, followed by a two-step soft baking for 7 min at 65 °C and 12 min at 95 °C. Then, a 70 µm thick photoresist film was produced (Figure 1d). A lithographic mask was pressed against the film, and a UV light was passed through this mask from the top side for 14 s (Figure 1e). Subsequently, the wafer was developed in a solution of propylene glycol monomethyl ether acetate (PGMEA) and rinsed in isopropanol (IPA) to dissolve the unexposed photoresist. Then the hierarchical microhole array was formed in the photoresist film as a mold (Figure 1f). PDMS with good replication capability and low cost was used as a filling material to duplicate the structures from the mold. It was mixed with pre-polymer PDMS and curing agent at a mass ratio of 10:1 and degassed for 10 min under vacuum. Then the photoresist mold was filled with the PDMS solution by spin coating process at 1500 rpm for 40 s, followed by putting in vacuum for 30 min to degas air in the structures (Figure 1g). Following this, the PDMS was cured for 2 h at 85 °C and demolding from the photoresist mold to obtain the PDMS hierarchical structure (Figure 1h). The thicknesses of the fabricated PDMS hierarchical structures were 70 µm. In the fabrication process of the hierarchical structures, the diameters and center distances of the secondary and primary micropillars could be controlled accurately and conveniently by regulating the masks' sizes. Therefore, the hierarchical structures could be well-controlled and scalable manufacturing, taking advantage of the high accuracy, large area, and high consistency of the used lithography and nanoimprinting technology.

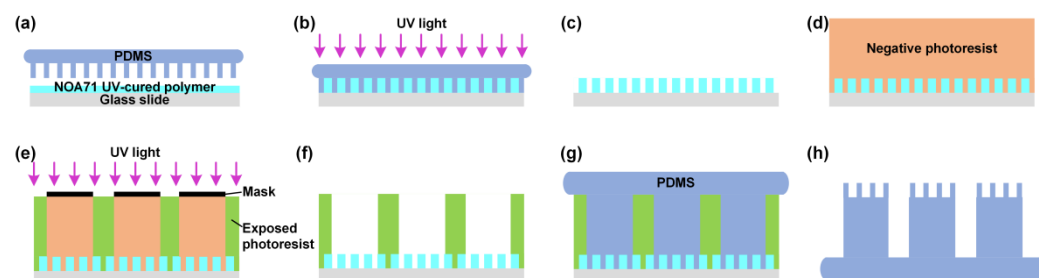


**Figure 1.** Schematic diagram of photolithography and micromolding process to fabricate hierarchical structures: (a–c) imprinting the secondary structure template, (d–f) forming the hierarchical microhole array by UV-lithography, (g,h) molding to obtain the PDMS hierarchical structure.

In our experiment, the diameter of the secondary and primary micropillars was set as 3 µm and 50 µm, respectively. The center distances of the secondary micropillars were controlled to be 6 µm and 9 µm, and the center distances of the primary micropillars were adjusted to be 100 µm, 150 µm, and 200 µm. For the convenience of description, the PDMS film is named as I-center distance of primary micropillars-II-center distance of secondary micropillars. For example, the I-150-II-9 represents the hierarchical PDMS film which possesses the primary micropillars with a center distance of 150 µm and the secondary micropillars with a center distance of 9 µm.

## 2.2. Fabrication of TENGs

A flexible and transparent ITO-PET film was used as the bottom electrode. It was firstly treated with oxygen plasma to enhance the adhesive strength. Then the fabricated flexible hierarchical structure was bonded with the ITO-PET film under a certain pressure to assemble a TENG device in single-electrode mode. A conductive tape was attached to the ITO-PET film as conducting wire to collect the triboelectric signals. A glass slide was used as a substrate to provide support from uncontrollable deformation under flowing water. The real photo and schematic illustration of the fabricated device are shown in Figure S2.

### 2.3. Characterizations and Measurements

A laser scanning confocal microscopy (Olympus LEXT OLS4000, Olympus: Tokyo, Japan) was employed to measure the thicknesses of the photoresist films, the thicknesses of the PDMS films, and the sizes of the hierarchical structures. The morphologies of the hierarchical structures were characterized using a field-emission scanning electron microscope (FESEM, Hitachi SU-8010, Hitachi: Tokyo, Japan). The static contact angles and the sliding angles of the hierarchical structures were measured by a contact angle measuring system (Dataphysics OCA20, Dataphysics: Filderstadt, Germany) with a deionized water droplet of 3  $\mu\text{L}$ . It is well known that surface modification using  $\text{C}_4\text{F}_8$  plasma to deposit a layer of  $\text{CF}_x$  polymer on PDMS could increase its hydrophobicity [34]. In our case, it was also found that after being treated with  $\text{C}_4\text{F}_8$  plasma for 60 s, the contact angle of the PDMS film with individual secondary micropillars (diameter: 3  $\mu\text{m}$ , center distance: 6  $\mu\text{m}$ ) increased from  $140^\circ$  to  $144^\circ$ . Therefore, prior to contact angle characterization and triboelectric output measurements, all samples were modified by  $\text{C}_4\text{F}_8$  plasma for 60 s.

For evaluating the output performance of water-solid contact TENGs, an oscilloscope (Tektronix DPO3034, Tektronix: Beaverton, OR, USA) with a  $100 \text{ M}\Omega$  probe (GENTEK G3100, GENTEK: Jiangsu, China) was employed to record the output voltage, and a low noise current preamplifier (SR570, Stanford Research Systems, SR570: Sunnyvale, CA, USA) was used to measure the short-circuit current.

## 3. Results and Discussion

### 3.1. Morphologies of Hierarchical Structures

SEM observed the morphologies of the hierarchical structures under different magnification levels. Figure 2a,b shows the SEM images of the PDMS hierarchical structures I-100-II-6 and I-150-II-9 (I represents the center distance of primary micropillars and II represents the center distance of secondary micropillars). It can be seen that in these two samples, the diameters of the primary and secondary micropillars were both 50  $\mu\text{m}$  and 3  $\mu\text{m}$ , while the center distances of the primary and secondary micropillars increased from 100  $\mu\text{m}$  to 150  $\mu\text{m}$  and 6  $\mu\text{m}$  to 9  $\mu\text{m}$ , respectively. For comparison, the individual primary structures were prepared when the UV-cured polymer microhole template substrate in Figure 1d was replaced by a flat glass slide. Figure 2c presents the morphology of the PDMS film I-150, which is only equipped with the primary micropillar array with a diameter of 50  $\mu\text{m}$  and a center distance of 150  $\mu\text{m}$ . During the fabrication process of the hierarchical structures, when just the first step, as shown in Figure S1, was conducted, the individual secondary structures were obtained. Figure 2d gives the SEM images of the PDMS film II-9, which owned the single secondary micropillar pattern with a diameter of 3  $\mu\text{m}$  and center distance of 9  $\mu\text{m}$ . These SEM images indicated the photolithography and micromolding process was an effective method to realize the controllable and scalable fabrication of the hierarchical structures. The fabricated two-level micropillars exhibited high accuracy and good consistency.

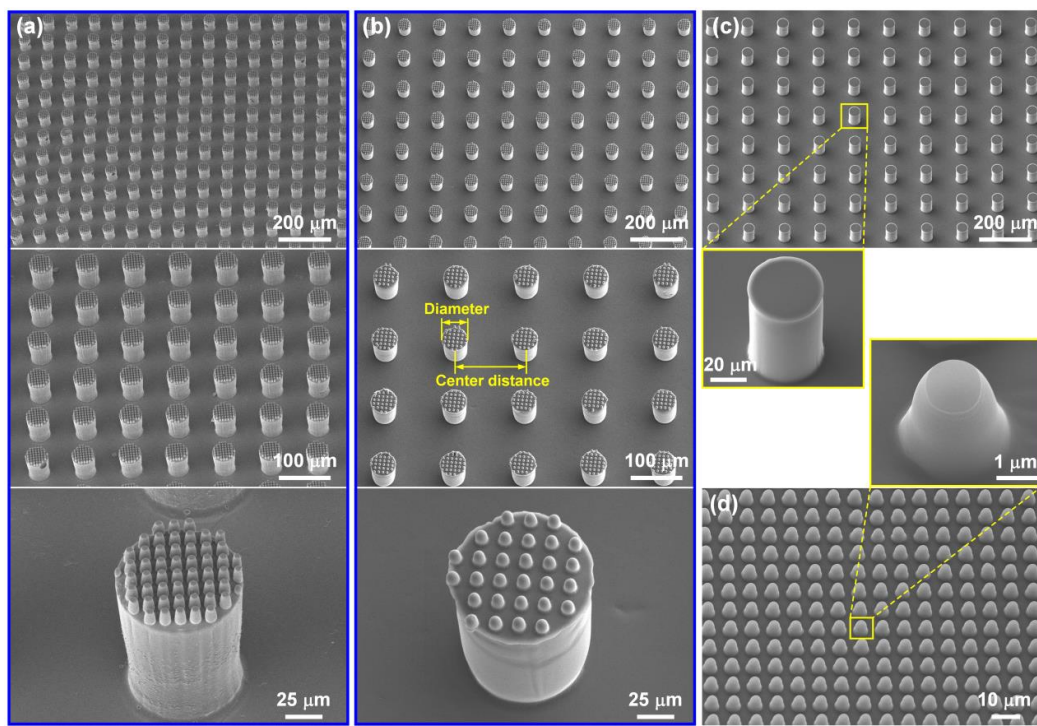


**Figure 2.** SEM images of the PDMS films: (a) hierarchical structure I-100-II-6, (b) hierarchical structure I-150-II-9, (c) individual primary structure I-150, and (d) individual secondary structure II-9.

### 3.2. Hydrophobic Performance of Hierarchical Structures

The hydrophobic characteristic was important for improving the water-energy harvesting performance for water-TENGs. Figure 3 presents the static contact angles of different PDMS films with a deionized water droplet of 3  $\mu\text{L}$ . All samples were treated with  $\text{C}_4\text{F}_8$  plasma before contact angle measurements. As shown in Figure 3a, the contact angles of the single primary structure I-150, the single secondary structure II-9, and the corresponding hierarchical structure I-150-II-9 were approximately  $149^\circ$ ,  $147^\circ$ , and  $164^\circ$ , respectively. For comparison, the flat PDMS film had a contact angle of  $100^\circ$ , as shown in Figure S3a. These results indicated that the constructed hierarchical structures exhibited a larger contact angle and superior hydrophobic property compared with the flat film and the single-level micropillar arrays. The hierarchical structure I-150-II-9 achieved superhydrophobicity considering that its contact angle exceeded  $150^\circ$ . The Cassie–Baxter equation could explain the phenomenon for hydrophobic surfaces. These PDMS films exhibited the Cassie–Baxter wetting state in which the water drop sits mostly on the structured surface filled with trapped air pockets but does not penetrate into the gaps of the micropillars. According to the Cassie–Baxter equation, the contact angle would increase with decreasing contact area [35,36]. Constructing a hierarchical structure would make the contact area between the film and water droplet decrease, finally showing a larger contact angle than the flat film and the single-level micropillar arrays and realizing superhydrophobicity.

Figure 3b,c compares the contact angles of the hierarchical PDMS films with different center distances to explore the effect of the structure parameter on the hydrophobic performance. It can be seen that compared with I-150-II-9, when the center distances of the secondary micropillars decreased to  $6 \mu\text{m}$ , the contact angle decreased to  $160^\circ$ , as shown in Figure 3b. The contact angle of the hierarchical structure I-100-II-9 also decreased to  $160^\circ$ , as shown in Figure 3c. It indicated that the contact angle decreased for the hierarchical structure I-150-II-9 as the center distances of either primary micropillars or secondary micropillars decreased. This is because the decrease of the micropillar center distance would make the contact area increase, ultimately reducing the contact angle of the hierarchical structures. The contact angles of the hierarchical structures with a secondary micropillar

center distance of 6  $\mu\text{m}$  showed a consistent changing tendency when regulating the primary micropillar center distance. As shown in Figure S4, when the center distance of the primary micropillars increased from 100  $\mu\text{m}$  to 150  $\mu\text{m}$  and 200  $\mu\text{m}$ , the contact angle of the hierarchical film showed an upward trend from 155° to 160° and 165° owing to the decreasing contact area.

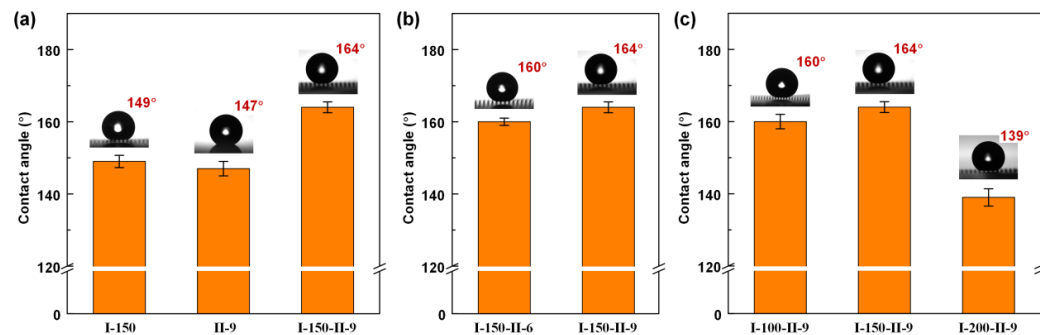


**Figure 3.** Contact angles of different PDMS films: (a) single primary structure I-150, single secondary structure II-9, and corresponding hierarchical structure I-150-II-9, (b) hierarchical structures with different secondary micropillar center distances, (c) hierarchical structures with different primary micropillar center distances.

However, it can also be found that the hierarchical structure I-200-II-9 had a lower contact angle of 139°, as shown in Figure 3c, which did not conform with the above rule. The reason was given as follows. The contact area would significantly decrease when the micropillar center distance was too large. Excessive micropillar gaps would be extremely easy to make the water drop sitting on the structured surface collapse and penetrate between the micropillar pattern. Then the surface would transform from Cassie–Baxter wetting state to Wenzel wetting state, in turn reducing the contact angle of the hierarchical structures [37,38].

In addition to static contact angle, sliding angle is another significant parameter to evaluate the hydrophobic property of the solid surface, and it also plays an important role in the triboelectric output of water-solid contact TENGs. This study found that the hierarchical structures under Cassie–Baxter wetting state, such as I-150-II-9, I-150-II-6, and I-100-II-6, all exhibited a sliding angle of less than 5°. While the flat PDMS film showed a sliding angle of 74°, as shown in Figure S3b. Compared with the flat film, the lower sliding angle for the hierarchical structures would make for the more and faster charge transfer when applied to water-TENGs through leading water drops to slide off rapidly and shortening the contacting and leaving period.

### 3.3. Application of Hierarchical Structures to Water-TENGs

Figure 4a presents the energy harvesting mechanism of the hierarchical structures-based water-TENGs. When the water droplets dripped onto the hierarchical structures (Figure 4(ai)), the contact electrification between water and PDMS would occur, and triboelectricity would be generated. According to the triboelectric series [39], the PDMS surface is highly electronegative, so charges would transfer from water to the PDMS films, making the PDMS hierarchical structures negatively charged and the droplets positively charged (Figure 4(aii)). When sufficient friction between water and PDMS took place, the PDMS surface would be accumulated a large number of negative charges. During the subsequent impact of the flowing water droplets, the contact area between water and the negatively charged hierarchical surface was dynamically varied, which would motivate an electrostatic induction and finally contribute to the triboelectric output. As shown in Figure 4(aiii), when fewer water droplets were in contact with the PDMS surface, some negative charges on the PDMS surface were compensated for by the attracted cations on the water surface, while others would drive electrons to flow from the bottom electrode

to ground until reaching equilibrium. When the contact area between the flowing water and the hierarchical structure continued to increase, as shown in Figure 4(aiv), the negative charges on the PDMS surface were purely compensated for by the cations of the water droplets. Electrons were attracted from the ground to the bottom electrode to neutralize the excessive positive charges on the bottom electrode. If water was dripped at a constant flow velocity, the contact area between water and PDMS would periodically decrease and increase. Then a loop from Figure 4(aiii) to Figure 4(aiv) would be induced, and an alternating electron flow in the external load would be observed.

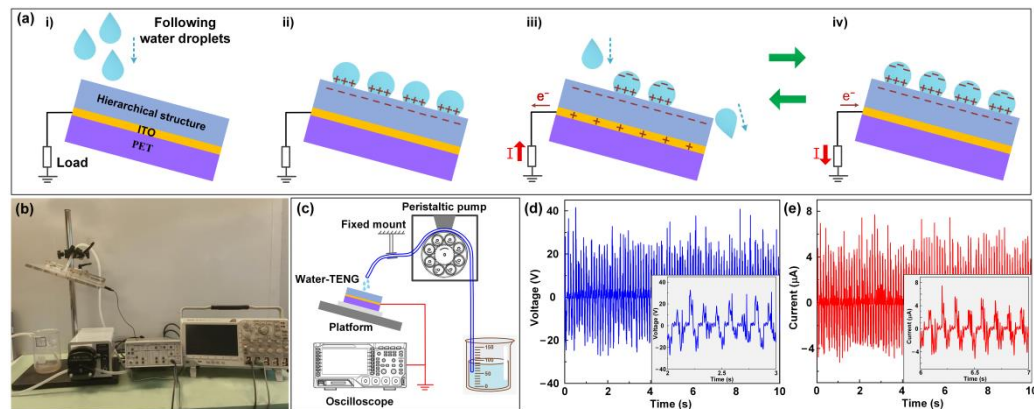


**Figure 4.** (a) Working mechanism of TENGs based on hierarchical structure and flowing water droplets. (b) Photograph and (c) schematic illustration of testing setup for water-TENGs. Typical output (d) voltage curve and (e) short-circuit current curve of the hierarchical structure-based water-TENG at a flowing velocity of 8 mL/s, the inset figures show the enlarged views.

Based on the working principle of water-TENGs, the testing setup of water dripping onto the PDMS hierarchical structure was constructed as shown in Figure 4b,c. The TENG device comprised of the PDMS hierarchical structure, and the bottom electrode was fixed on a support platform with an inclined angle of 15°. Water was pumped by a peristaltic pump to drip from a height of 3.5 cm onto the hierarchical structure. The peristaltic pump can control the flow velocity of the water droplets. The output voltage and current were recorded using an oscilloscope and a current preamplifier. The inherent impedance of the TENG device is generally in the range of hundreds of MΩ [40]. The noise level of the device for output voltage measurement was nearly 3 V, as shown in Figure S5. Figure 4d,e presents the typical output voltage and current curves generated from the hierarchical structure-based water-TENG at a flowing velocity of 8 mL/s. The fluctuation of the triboelectric outputs was attributed to the irregular change in the contact area between water and the hierarchical structure.

In order to study the effect of the film structure on the water-energy harvesting capacity, the output performance of water-TENGs based on the PDMS films with different morphologies at a flowing velocity of 8 mL/s is compared as shown in Figure 5a,b. Compared with the flat film, the single primary structure I-150, and the single secondary structure II-9, the corresponding hierarchical structure I-150-II-9 presented the enhanced output response. Its output voltage reached approximately 34 V, and the short-circuit current achieved around 5 μA. These results demonstrated that the construction of the hierarchical structures could enhance the ability of water-TENGs to harvest water energy. The reason was suggested as follows. Firstly, establishing hierarchical structures could increase the surface area of the triboelectric layer, and more charges would be generated during the contact electrification process. The higher charge density in the triboelectric layer could effectively enhance the output performance of TENG. Secondly, the fabrication of the hierarchical structures reinforced the hydrophobic property and achieved the superhydrophobic surface, which was essential for water-TENGs to harvest water energy. When the insufficient hydrophobic films were used as the triboelectric layer of water-TENGs, more water droplets would

remain on the sample surface to form a layer of water, eventually screening some negative charges in the triboelectric layer and weakening the electric output. The superhydrophobic hierarchical surface could avoid forming a residual water film under flowing water. A sliding angle of less than 5° also facilitated the complete slide off of the water droplets. Owing to the increased amount of the water drops which took part in the contacting and leaving with the hierarchical structure, the change of the contact area would increase, ultimately resulting in higher output performance.

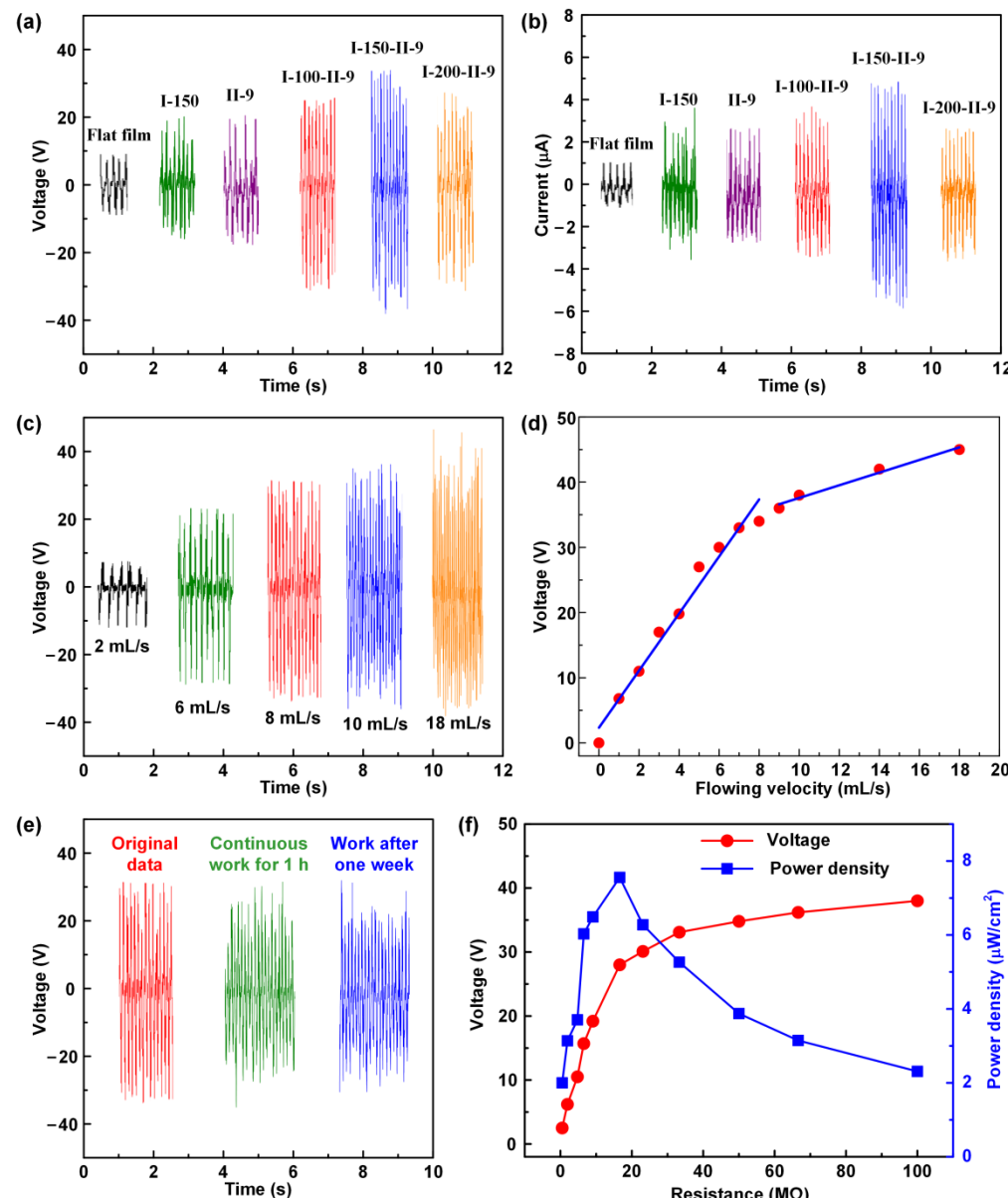


**Figure 5.** Output performance of water-solid contact TENGs. (a) Output voltage and (b) short-circuit current of water-TENGs based on the PDMS films with different morphologies at a flowing velocity of 8 mL/s. (c) Output voltages of the hierarchical structure I-150-II-9-based water-TENG at different flowing velocities. (d) Relationship between the output voltage and flowing velocity of the hierarchical structure I-150-II-9-based water-TENG. (e) Output voltages of the water-TENG device after continuous work for 1 h and when the test was conducted again after being placed for one week. (f) Output voltage and power density curve across different resistive loads for the hierarchical structure I-150-II-9-based water-TENG device at a flowing velocity of 10 mL/s.

In addition, when the secondary micropillar center distance was set as 9  $\mu\text{m}$ , the output responses of the hierarchical structures as the primary micropillar center distance changed are also compared in Figure 5a,b. It was found that the variation tendency of the electric output was in accord with the contact angle. As the contact angle increased, the hydrophobic property enhanced. The outstanding hydrophobicity resulted in more water drops bouncing off the surface and a greater change in the contact area, which played a vital role in harvesting water energy for water-TENGs. When the primary micropillar center distance was 100  $\mu\text{m}$  and 150  $\mu\text{m}$ , the hierarchical surfaces presented the Cassie–Baxter wetting state, and the flowing water drops would not penetrate into the micropillar gaps but rapidly slide off, which was beneficial to the charge transfer. In contrast, the hierarchical surface I-200-II-9 exhibited the Wenzel wetting state in which the flowing water would immerse into the micropillar arrays. The immersed water film would neutralize some negative charges of the hierarchical surface, leading to a lower output.

Furthermore, the effect of the flowing velocity on the output performance was also analyzed. Figure 5c shows the output voltage of the hierarchical structure I-150-II-9-based water-TENG at the flowing velocities between 2 mL/s and 18 mL/s. And Figure 5d fits the relationship between output voltage and flowing velocity of the hierarchical structure I-150-II-9-based water-TENG. It can be seen that as the flowing velocity increased from 0 mL/s to  $\sim$ 8 mL/s, the output voltage increased remarkably. The reason was suggested to be that the increase of the flowing velocity would induce more triboelectricity in the hierarchical surface. The charge density increase in the triboelectric layer would contribute to higher output. When the flowing velocity continued to increase from  $\sim$ 8 mL/s to 18 mL/s, the slope of the fitting curve decreased, and the output voltage tended to saturate. When the flowing velocity increased to a certain degree, the contact between the hierarchical structure and the water was sufficient, and the induced triboelectricity became saturated, resulting in the decline in the increasing tendency. Meanwhile, it was found that the output frequency also increased with the flowing velocity. The increase of the flowing velocity would accelerate the contacting and leaving process of water and the hierarchical structure, motivating the faster charging and discharging speed. These results endowed the hierarchical structures-based water-TENGs with the potential to apply to a self-powered sensor for measuring the flow velocity within a certain range. In addition, the hitting angle of the water droplets is also an important factor that affects the triboelectric output. Mariello et al. have reported that as the inclination angle of the TENG plane with respect to the water flow direction increased from 0° to 90°, the output voltage increased [26]. When the hitting angle of the flowing water increased, more kinetic energy from the impact of the flowing water would be transferred to the water-TENG, resulting in a larger degree of contact electrification and a higher triboelectric output. The cycle stability and device stability were also studied. As shown in Figure 5e, no obvious degradation of the output voltage was measured after continuous work for 1 h. It even maintained high performance when the test was conducted again after the device was placed for one week in the open environment. These results indicated that the water-TENG device had excellent durability and could be used for long-term practical purposes.

Moreover, the power density of the hierarchical structure-based water-TENG device was analyzed. At a flowing velocity of 10 mL/s, the water-TENG based on the hierarchical structure I-150-II-9 was connected with different resistive loads. Then the voltages were measured, and the power densities were calculated. The result is presented in Figure 5f, and the water-TENG device exhibited a power density peak of 7.56  $\mu\text{W}/\text{cm}^2$  at 16.6 M $\Omega$ . Table 1 summarizes the comparison of this work with other water-TENGs reported in the literature in terms of material used, contact angle, and output performances [23,26,28,41–44]. Our proposed water-TENG device exhibited good output power generation and robust durability, which endowed the hierarchical structure-based water-TENG with good potential applications in water energy harvesting and self-powered sensor devices [45,46].

**Table 1.** Comparison of many water-TENGs in terms of materials used, contact angle, and output performances.

Tribolayer Materials Used in Water-TENG	Contact Angle	Energy Source	Voltage	Current	Power Density or Power	Stability	Ref.
SiO <sub>2</sub> /P(VDF-TrFE) hierarchical micro-nanostructures	158.1°	Flowing water with a velocity of 10.7 mL/s	36 V	10 μA	/	/	[28]
Modified layered double hydroxides	159°	Flowing water with a velocity of 92 mL/min	13 V	1.6 μA/cm <sup>2</sup>	~300 nW/cm <sup>2</sup>	7000 s	[41]
PVDF	124°	Flowing water	20.92 V	0.95 μA	26.53 mW/m <sup>2</sup>	1 h	[42]
Parylene C surface-treated with UV/ozone	/	Flowing water with a velocity of 3.33 mL/s	2 V	/	9 mW/m <sup>2</sup>	/	[26]
PTFE film with hierarchical micro-/nanostructures	169°	Water drops	9.3 V	17 μA	145 μW	/	[23]
		Flowing water with a velocity of 30 mL/s	/	1.5 μA/cm <sup>2</sup>	20 mW/cm <sup>2</sup>	/	
rGO@PDMS	116.9°	Water drops	~2 V	~2 nA	/	/	[43]
Fluorocarbon/silica coating	156°	Water drops	20 V	4.5 μA	/	/	[44]
PDMS hierarchical structures	164°	Flowing water with a velocity of 8–10 mL/s	34 V	5 μA	7.56 μW/cm <sup>2</sup>	1 h	This work

#### 4. Conclusions

A controllable and scalable fabrication approach for the superhydrophobic hierarchical structures was developed, and the hierarchical surface was demonstrated to effectively harvest water energy when applied to the water-solid contact TENGs. The lithography and nanoimprinting technology manufactured the hierarchical structures with two-level micropillar arrays. The diameters and center distances of the hierarchical micropillars could be regulated accurately and conveniently by changing the size of the masks. The fabricated two-level micropillars exhibited high accuracy and good consistency. Then the hydrophobic properties of the single-level and hierarchical structures were compared, and the results indicated that the hierarchical surface exhibited a larger contact angle and realized superhydrophobicity. Specifically, the hierarchical structure I-150-II-9 showed a contact angle of 164° and a sliding angle of less than 5°. Afterward, the hierarchical structures were applied to water-TENGs with flowing water continuously dripping on, and the effect of the structure parameter on the triboelectric output was analyzed. The hierarchical structures-based water-TENGs presented more outstanding triboelectric output than the flat film and single-level structures due to the enhanced friction area and superhydrophobic property. In addition, the effect of the primary micropillar center distance on the output performance of water-TENGs was found to be consistent with the change of the hydrophobic property, demonstrating the significant contribution of superhydrophobicity to water energy harvesting. At a flowing velocity of 8 mL/s, the hierarchical structure I-150-II-9 generated the output voltage of approximately 34 V and the short-circuit current of around 5 μA. The water-TENG device exhibited a power density peak of 7.56 μW/cm<sup>2</sup> with a resistive load of 16.6 MΩ at a flowing velocity of 10 mL/s. These findings shed light on the potential applications of the hierarchical structures-based water-TENGs to water energy harvesting and self-powered sensor devices.

**Supplementary Materials:** The following supporting information can be downloaded at: <https://www.mdpi.com/article/10.3390/electronics11101651/s1>, Figure S1: Schematic illustration of PDMS secondary structure fabrication process; Figure S2: (a) Photo and (b) schematic illustration of

the fabricated TENG device; Figure S3: (a) Static contact angle and (b) sliding angle of the flat PDMS film; Figure S4: Contact angles of the hierarchical structures with a secondary micropillar center distance of 6  $\mu\text{m}$ ; Figure S5: Noise level of the water-TENG device for output voltage measurement.

**Author Contributions:** Conceptualization, M.G. and Z.Y.; Formal analysis, P.L.; Funding acquisition, P.L. and Q.W.; Investigation, C.W. and Z.X.; Project administration, M.Y.; Supervision, Y.L.; Validation, Y.Z. and Q.W.; Visualization, C.W. and P.Z.; WritingOriginal draft, M.G.; Writing–Review & editing, Z.Y. and Y.L. All authors have read and agreed to the published version of the manuscript.

**Funding:** This research was funded by the National Natural Science Foundation of China (Grant Numbers. 51905423, 52075437, 52075439, and 51775431) and the Natural Science Basic Research Plan in Shaanxi Province of China (Grant Numbers. 2022JM-244 and 2021JM-338).

**Conflicts of Interest:** The authors declare no conflict of interest.

## References

- Wang, Z.L.; Chen, J.; Lin, L. Progress in triboelectric nanogenerators as a new energy technology and self-powered sensors. *Energy Environ. Sci.* **2015**, *8*, 2250–2282. [[CrossRef](#)]
- Xiong, J.; Thangavel, G.; Wang, J.; Zhou, X.; Lee, P.S. Self-healable sticky porous elastomer for gas-solid interacted power generation. *Sci. Adv.* **2020**, *6*, eabb4246. [[CrossRef](#)] [[PubMed](#)]
- Chen, X.; Parida, K.; Wang, J.; Xiong, J.; Lin, M.F.; Shao, J.; Lee, P.S. A stretchable and transparent nanocomposite nanogenerator for self-powered physiological monitoring. *ACS Appl. Mater. Interfaces* **2017**, *9*, 42200–42209. [[CrossRef](#)] [[PubMed](#)]
- Fan, F.R.; Tang, W.; Wang, Z.L. Flexible nanogenerators for energy harvesting and self-powered electronics. *Adv. Mater.* **2016**, *28*, 4283–4305. [[CrossRef](#)] [[PubMed](#)]
- Xiong, J.; Cui, P.; Chen, X.; Wang, J.; Parida, K.; Lin, M.F.; Lee, P.S. Skin-touch-actuated textile-based triboelectric nanogenerator with black phosphorus for durable biomechanical energy harvesting. *Nat. Commun.* **2018**, *9*, 4280. [[CrossRef](#)]
- Bhunia, S.; Chandel, S.; Karan, S.K.; Dey, S.; Tiwari, A.; Das, S.; Kumar, N.; Chowdhury, R.; Mondal, S.; Ghosh, I.; et al. Autonomous self-repair in piezoelectric molecular crystals. *Science* **2021**, *373*, 321–327. [[CrossRef](#)]
- Si, S.K.; Paria, S.; Karan, S.K.; Ojha, S.; Das, A.K.; Maitra, A.; Bera, A.; Halder, L.; De, A.; Khatua, B.B. In situ-grown organo-lead bromide perovskite-induced electroactive  $\gamma$ -phase in aerogel PVDF films: An efficient photoactive material for piezoelectric energy harvesting and photodetector applications. *Nanoscale* **2020**, *12*, 7214–7230. [[CrossRef](#)]
- Paria, S.; Bera, R.; Karan, S.K.; Maitra, A.; Das, A.K.; Si, S.K.; Halder, L.; Bera, A.; Khatua, B.B. Insight into cigarette wrapper and electroactive polymer based efficient TENG as biomechanical energy harvester for smart electronic applications. *ACS Appl. Energy Mater.* **2018**, *1*, 4963–4975. [[CrossRef](#)]
- Wang, X.; He, Y.; Liu, X. Synchronous steam generation and photodegradation for clean water generation based on localized solar energy harvesting. *Energy Convers. Manag.* **2018**, *173*, 158–166. [[CrossRef](#)]
- Fan, F.R.; Tian, Z.Q.; Wang, Z.L. Flexible triboelectric generator. *Nano Energy* **2012**, *1*, 328–334. [[CrossRef](#)]
- Zhou, J.; Wang, H.; Du, C.; Zhang, D.; Lin, H.; Chen, Y.; Xiong, J. Cellulose for Sustainable Triboelectric Nanogenerators. *Adv. Energy Sustain. Res.* **2021**, *3*, 2100161. [[CrossRef](#)]
- Zhang, W.; Wang, P.; Sun, K.; Wang, C.; Diao, D. Intelligently detecting and identifying liquids leakage combining triboelectric nanogenerator based self-powered sensor with machine learning. *Nano Energy* **2019**, *56*, 277–285. [[CrossRef](#)]
- Jia, C.; Zhu, Y.; Sun, F.; Zhao, T.; Xing, R.; Mao, Y.; Zhao, C. A Flexible and Stretchable Self-Powered Nanogenerator in Basketball Passing Technology Monitoring. *Electronics* **2021**, *10*, 2584. [[CrossRef](#)]
- Bai, P.; Zhu, G.; Lin, Z.H.; Jing, Q.; Chen, J.; Zhang, G.; Ma, J.; Wang, Z.L. Integrated multilayered triboelectric nanogenerator for harvesting biomechanical energy from human motions. *ACS Nano* **2013**, *7*, 3713–3719. [[CrossRef](#)] [[PubMed](#)]
- Tang, G.; Cheng, F.; Hu, X.; Huang, B.; Xu, B.; Li, Z.; Yan, X.; Yuan, D.; Wu, W.; Shi, Q. A two-degree-of-freedom cantilever-based vibration triboelectric nanogenerator for low-frequency and broadband operation. *Electronics* **2019**, *8*, 1526. [[CrossRef](#)]
- Zhang, L.; Zhang, B.; Chen, J.; Jin, L.; Deng, W.; Tang, J.; Zhang, H.; Pan, H.; Zhu, M.; Yang, W.; et al. Lawn structured triboelectric nanogenerators for scavenging sweeping wind energy on rooftops. *Adv. Mater.* **2016**, *28*, 1650–1656. [[CrossRef](#)]
- Jiang, D.; Xu, M.; Dong, M.; Guo, F.; Liu, X.; Chen, G.; Wang, Z.L. Water-solid triboelectric nanogenerators: An alternative means for harvesting hydropower. *Renew. Sustain. Energy Rev.* **2019**, *115*, 109366. [[CrossRef](#)]
- Yang, L.; Wang, Y.; Guo, Y.; Zhang, W.; Zhao, Z. Robust working mechanism of water droplet-driven triboelectric nanogenerator: Triboelectric output versus dynamic motion of water droplet. *Adv. Mater. Interfaces* **2019**, *6*, 1901547. [[CrossRef](#)]
- Kwon, D.H.; Kwon, J.H.; Jeong, J.; Lee, Y.; Biswas, S.; Lee, D.W.; Lee, S.; Bae, J.H.; Kim, H. Textile Triboelectric Nanogenerators with Diverse 3D-Spacer Fabrics for Improved Output Voltage. *Electronics* **2021**, *10*, 937. [[CrossRef](#)]
- Jin, S.; Wang, Y.; Motlag, M.; Gao, S.; Xu, J.; Nian, Q.; Wu, W.; Cheng, G.J. Large-area direct laser-shock imprinting of a 3D biomimic hierarchical metal surface for triboelectric nanogenerators. *Adv. Mater.* **2018**, *30*, 1705840. [[CrossRef](#)]
- Huang, Y.; Ding, Y.; Bian, J.; Su, Y.; Zhou, J.; Duan, Y.; Yin, Z. Hyper-stretchable self-powered sensors based on electrohydrodynamically printed, self-similar piezoelectric nano/microfibers. *Nano Energy* **2017**, *40*, 432–439. [[CrossRef](#)]

22. Wu, X.; Li, X.; Ping, J.; Ying, Y. Recent advances in water-driven triboelectric nanogenerators based on hydrophobic interfaces. *Nano Energy* **2021**, *90*, 106592. [CrossRef]
23. Lin, Z.H.; Cheng, G.; Lee, S.; Pradel, K.C.; Wang, Z.L. Harvesting water drop energy by a sequential contact-electrification and electrostatic-induction process. *Adv. Mater.* **2014**, *26*, 4690–4696. [CrossRef] [PubMed]
24. Lee, J.H.; Kim, S.; Kim, T.Y.; Khan, U.; Kim, S.W. Water droplet-driven triboelectric nanogenerator with superhydrophobic surfaces. *Nano Energy* **2019**, *58*, 579–584. [CrossRef]
25. Hu, S.; Shi, Z.; Zheng, R.; Ye, W.; Gao, X.; Zhao, W.; Yang, G. Superhydrophobic liquid–solid contact triboelectric nanogenerator as a droplet sensor for biomedical applications. *ACS Appl. Mater. Interfaces* **2020**, *12*, 40021–40030. [CrossRef]
26. Mariello, M.; Fachechi, L.; Guido, F.; De Vittorio, M. Multifunctional sub-100  $\mu\text{m}$  thickness flexible piezo/triboelectric hybrid water energy harvester based on biocompatible AlN and soft parylene C-PDMS-Ecoflex<sup>TM</sup>. *Nano Energy* **2021**, *83*, 105811. [CrossRef]
27. Zhang, J.H.; Hao, X. Enhancing output performances and output retention rates of triboelectric nanogenerators via a design of composite inner-layers with coupling effect and self-assembled outer-layers with superhydrophobicity. *Nano Energy* **2020**, *76*, 105074. [CrossRef]
28. Chen, X.; Xiong, J.; Parida, K.; Guo, M.; Wang, C.; Wang, C.; Li, X.; Shao, J.; Lee, P.S. Transparent and stretchable bimodal triboelectric nanogenerators with hierarchical micro-nanostructures for mechanical and water energy harvesting. *Nano Energy* **2019**, *64*, 103904. [CrossRef]
29. Ahn, J.; Zhao, Z.J.; Choi, J.; Jeong, Y.; Hwang, S.; Ko, J.; Gu, J.; Jeon, S.; Park, J.; Kang, M.; et al. Morphology-controllable wrinkled hierarchical structure and its application to superhydrophobic triboelectric nanogenerator. *Nano Energy* **2021**, *85*, 105978. [CrossRef]
30. Zou, Y.; Xu, J.; Chen, K.; Chen, J. Advances in nanostructures for high-performance triboelectric nanogenerators. *Adv. Mater. Technol.* **2021**, *6*, 2000916. [CrossRef]
31. Zhou, Q.; Lee, K.; Kim, K.N.; Park, J.G.; Pan, J.; Bae, J.; Baik, J.M.; Kim, T. High humidity- and contamination-resistant triboelectric nanogenerator with superhydrophobic interface. *Nano Energy* **2019**, *57*, 903–910. [CrossRef]
32. Cho, H.; Chung, J.; Shin, G.; Sim, J.Y.; Kim, D.S.; Lee, S.; Hwang, W. Toward sustainable output generation of liquid–solid contact triboelectric nanogenerators: The role of hierarchical structures. *Nano Energy* **2019**, *56*, 56–64. [CrossRef]
33. Lin, Z.H.; Cheng, G.; Wu, W.; Pradel, K.C.; Wang, Z.L. Dual-mode triboelectric nanogenerator for harvesting water energy and as a self-powered ethanol nanosensor. *ACS Nano* **2014**, *8*, 6440–6448. [CrossRef] [PubMed]
34. Kim, Y.G.; Lim, N.; Kim, J.; Kim, C.; Lee, J.; Kwon, K.H. Study on the surface energy characteristics of polydimethylsiloxane (PDMS) films modified by  $\text{C}_4\text{F}_8/\text{O}_2/\text{Ar}$  plasma treatment. *Appl. Surf. Sci.* **2019**, *477*, 198–203. [CrossRef]
35. Erbil, H.Y.; Cansoy, C.E. Range of applicability of the Wenzel and Cassie-Baxter equations for superhydrophobic surfaces. *Langmuir* **2009**, *25*, 14135–14145. [CrossRef]
36. Cansoy, C.E.; Erbil, H.Y.; Akar, O.; Akin, T. Effect of pattern size and geometry on the use of Cassie–Baxter equation for superhydrophobic surfaces. *Colloids Surf. A* **2011**, *386*, 116–124. [CrossRef]
37. Murakami, D.; Jinnai, H.; Takahara, A. Wetting transition from the Cassie–Baxter state to the Wenzel state on textured polymer surfaces. *Langmuir* **2014**, *30*, 2061–2067. [CrossRef]
38. Lee, E.; Kim, D.H. Simple fabrication of asphalt-based superhydrophobic surface with controllable wetting transition from Cassie–Baxter to Wenzel wetting state. *Colloids Surf. A* **2021**, *625*, 126927. [CrossRef]
39. Wang, Z.L. Triboelectric nanogenerators as new energy technology for self-powered systems and as active mechanical and chemical sensors. *ACS Nano* **2013**, *7*, 9533–9557. [CrossRef]
40. Yi, F.; Wang, J.; Wang, X.; Niu, S.; Li, S.; Liao, Q.; Xu, Y.; You, Z.; Zhang, Y.; Wang, Z.L. Stretchable and waterproof self-charging power system for harvesting energy from diverse deformation and powering wearable electronics. *ACS Nano* **2016**, *10*, 6519–6525. [CrossRef]
41. Cui, P.; Wang, J.; Xiong, J.; Li, S.; Zhang, W.; Liu, X.; Gu, G.; Guo, J.; Zhang, B.; Cheng, G.; et al. Meter-scale fabrication of water-driven triboelectric nanogenerator based on in-situ grown layered double hydroxides through a bottom-up approach. *Nano Energy* **2020**, *71*, 104646. [CrossRef]
42. Cheedarala, R.K.; Shahriar, M.; Ahn, J.H.; Hwang, J.Y.; Ahn, K.K. Harvesting liquid stream energy from unsteady peristaltic flow induced pulsatile Flow-TENG (PF-TENG) using slipping polymeric surface inside elastomeric tubing. *Nano Energy* **2019**, *65*, 104017. [CrossRef]
43. Parvez, A.N.; Rahaman, M.H.; Kim, H.C.; Ahn, K.K. Optimization of triboelectric energy harvesting from falling water droplet onto wrinkled polydimethylsiloxane-reduced graphene oxide nanocomposite surface. *Compos. Part B* **2019**, *174*, 106923. [CrossRef]
44. Niu, J.; Xu, W.; Tian, K.; He, G.; Huang, Z.; Wang, Q. Triboelectric energy harvesting of the superhydrophobic coating from dropping water. *Polymers* **2020**, *12*, 1936. [CrossRef]
45. Huang, B.; Wang, P.; Wang, L.; Yang, S.; Wu, D. Recent advances in ocean wave energy harvesting by triboelectric nanogenerator: An overview. *Nanotechnol. Rev.* **2020**, *9*, 716–735. [CrossRef]
46. Mariello, M. Recent Advances on Hybrid Piezo-Triboelectric Bio-Nanogenerators: Materials, Architectures and Circuitry. *Nanoenergy Adv.* **2022**, *2*, 64–109. [CrossRef]